E-HIPA: An Energy-Efficient Framework for High-Precision Multi-Target-Adaptive Device-Free Localization

Ju Wang, Dingyi Fang, Zhe Yang, *Member, IEEE*, Hongbo Jiang, *Senior Member, IEEE*, Xiaojiang Chen, Tianzhang Xing, and Lin Cai, *Senior Member, IEEE*

Abstract—Device-free localization (DFL), which does not require any devices to be attached to target(s), has become an appealing technology for many applications, such as intrusion detection and elderly monitoring. To achieve high localization accuracy, most recent DFL methods rely on collecting a large number of received signal strength (RSS) changes distorted by target(s). Consequently, the incurred high energy consumption renders them infeasible for resource-constraint networks, such as wireless sensor networks. This paper introduces an energy-efficient framework for high-precision multi-target-adaptive device-free localization (E-HIPA). Compared with the existing methods, E-HIPA demands fewer transceivers, applies the compressive sensing (CS) theory to guarantee high localization accuracy with less RSS change measurements. The motivation behind the proposed E-HIPA is the sparse nature of multi-target locations in the spatial domain. Before taking advantage of this intrinsic sparseness, we theoretically prove the validity of the proposed CS-based framework problem formulation. Based on the formulation, the proposed E-HIPA primarily includes an adaptive orthogonal matching pursuit (AOMP) algorithm, by which it is capable of recovering the precise location vector with high probability, even for a more practical scenario with unknown target number. Experimental results via real testbed demonstrate that, compared with the previous state-of-the-art solutions, i.e., RTI, SCPL, and RASS approaches, E-HIPA reduces the energy consumption by up to 69 percent with meter-level localization accuracy.

Index Terms—Compressive sensing, energy-efficient, device-free localization

1 Introduction

Localization has long been playing one of the key roles in our daily life. Example applications include finding the lost object [1], time synchronization [2], [3] and routing design [4]. Extensive researches have been done to address the localization problem with the deployment of radio-frequency (RF) based devices/systems, for example, the Wi-Fi based indoor navigation [5]. Current localization systems typically localize the target when it carries devices. These systems may not be applicable in some scenarios. For instance, for the intrusion detection, it is impossible to pre-install the tracking devices on the intruders [6], [7], [8], [9], [10]. Therefore, device-free localization (DFL), which does not require any devices being attached to target(s), has become an appealing technology. Unlike previous works [6], [7], [8] which have focused on single target localization, this work aims at the multi-target DFL for applications ranging from customer activity mining in shopping malls [6] to intrusion detection [7], [8].

There are three types of DFL approaches for multiple targets,[1] based on how they utilize the received signal strength (RSS) changes[2] to localize the targets, including geometry based approaches [6], fingerprinting based approaches [11], [13] and radio tomographic imaging (RTI) based approaches [8]. The geometry based approaches, however, identify the locations of targets only using the geometric information[3] of distorted wireless links, which can be several meters, as shown in Fig. 1a. The fingerprinting based approaches can localize targets accurately by matching the most possible locations with the prior obtained fingerprints.[4] However, these approaches fail to localize multiple targets that stay within a single region, because they treat multiple targets as a single target, as illustrated in Fig. 1b. The RTI system [8]

- *J. Wang, D. Fang, X. Chen, and T. Xing are with the School of Information Science and Technology, Northwest University, Xi'an, China. E-mail: {wangju, dyf, xjchen, xtz}@nwu.edu.cn.*
- *Z. Yang is with the School of Computer Science, Northwestern Polytechnical University, Xi'an, China. E-mail: zyang@nwpu.edu.cn.*
- *H. Jiang is with School of Electronic Information and Communications, Huazhong University of Science and Technology, Wuhan, China. E-mail: hongbojiang2004@gmail.com.*
- *L. Cai is with the Department of Electrical & Computer Engineering, University of Victoria, Victoria, BC, Canada. E-mail: cai@ece.uvic.ca.*

Manuscript received 11 Feb. 2015; revised 21 Nov. 2015; accepted 28 Apr. 2016. Date of publication 12 May 2016; date of current version 2 Feb. 2017. For information on obtaining reprints of this article, please send e-mail to: reprints@ieee.org, and reference the Digital Object Identifier below. Digital Object Identifier no. 10.1109/TMC.2016.2567396

1. Some high-precision DFL systems, such as WiTrack2.0 [7] and Tadar [12], have been proposed; they demand dedicated hardware which can be costly in some scenarios. While, the RSS readings are readily available in existing commercial off-the-shelf transceivers. Thus, this study focuses on the RSS based DFL.

2. In general, a wireless communication link would be distorted if a target blocks part or all of the signal propagation paths. Thus, the value of the measured RSS will change compared with the case of no target presents. Such a change of the RSS value is defined as the RSS change.

3. Geometric information can be the midpoint of a link, the intersecting points of some links or the coverage area of a link [6].

4. A fingerprint is a mark made by the location on the distorted RSS measurement.

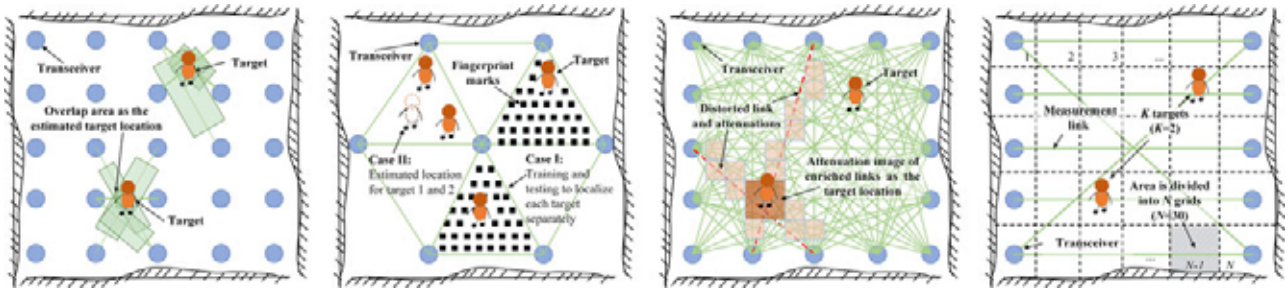

(a) Geometry based DFL. (b) Fingerprinting based DFL. (c) RTI-based DFL. (d) E-HIPA.

Fig. 1. An illustration of current approaches/systems and the proposed E-HIPA method for localizing two targets. (a) The geometry based best cover approach [6] considers the overlapped coverage area of distorted links as the target location. (b) The fingerprinting-based real-time accurate and scalable system (RASS) [11] localizes each target accurately in the separated triangles with prior obtained fingerprints (Case I); however, it fails to localize multiple targets even when targets located sparsely in the same triangle (Case II). (c) The RTI-based approach estimates a target location as an attenuation image of the enriched links and achieves an improved accuracy; however, it requires any pair of transceivers to communicate with each other, which leads to a high energy costs. (d) E-HIPA leverages the advantage of CS in sparse recovery to localize targets accurately with reduced transceivers and measurements; thus, the proposed E-HIPA achieves both the high-precision and energy-efficiency properties.

uses many wireless links traveling through the monitoring area to improve the localization performance for multiple targets. However, this improvement comes at the expense of a large volume of transmissions and high energy consumption, as it requires lots of transceivers to send and receive RSS measurements, as shown in Fig. 1c.

Considering a low energy cost is critical to prolong the system lifetime and thus can make the DFL approach/system practical, considering that most of the DFL systems are only composed of the energy-constrained wireless transceivers [14]. For example, the transceivers used in the RASS [11] and RTI [8] systems are wireless sensors, which rely on battery power [15]. Furthermore, from an operator's perspective, energy efficiency has significant economic benefits. Thus, one of the key problems in designing a DFL framework is how to *reduce the energy consumption* for the precisely localization of multiple targets.

This paper introduces an energy-efficient framework for high-precision multi-target-adaptive device-free localization (E-HIPA). The proposed E-HIPA achieves both the energy-efficiency and high-precision properties. First, by reducing the number of transceivers deployed in the monitoring area, as shown in Fig. 1d, the data volume and the energy consumption can be significantly reduced. However, the localization accuracy of traditional methods is bound to decrease when the number of transceivers is reduced. For example, J. Wilson et al. [16] showed that the localization errors of RTI increased 45 percent when the number of transceivers is decreased by 20 percent. Unlike previous work, E-HIPA utilises the compressive sensing (CS) theory to guarantee the high localization accuracy even with a small number of measurements (or transceivers). The main intuition to leverage the CS theory stems from the sparse nature of multi-target locations in the spatial domain, i.e., the number of multiple targets, K, is often small compared with the number of possible locations, N, in the monitoring area. This means that a location vector Θ which contains the location information of K targets is an ideal K-sparse signal[5] when the targets appear randomly in the monitoring area. Accordingly, by taking advantage of the CS theory for accurate recovery of sparse signals, E-HIPA localizes multiple targets accurately with a few measurements, i.e., it incurs very low energy cost.

In line with the common practice in localizing multiple targets [8], [11], [13], [17], the procedure of E-HIPA includes two building blocks. First, while one target moves around the monitoring area, we collect the RSS change values distorted by the target for each location as a fingerprint. In aggregate, fingerprints for all the locations make up a sensing matrix for this monitoring area. Second, to localize the target(s), both the current RSS measurements and the sensing matrix are required. Then, a CS recovery algorithm is applied to estimate the locations of the target(s). Two main challenges remain to apply CS in E-HIPA. *First*, although fingerprints are easy to obtain, it is unknown how to organize the fingerprints to form a sensing matrix that satisfies the restricted isometry property (RIP) [18], which is the basis to enable CS-based approaches. *Second*, to solve this CS-based framework problem formulation, i.e., to recover the location vector Θ, most current recovery algorithms presume the availability of the number of targets K, which unfortunately is an unknown parameter in most realistic scenarios. To deal with the first challenge, we analyze the characteristics of the row and column vectors of the sensing matrix. Accordingly, we define a rule for how to establish the sensing matrix and prove that the designed sensing matrix satisfies the RIP, thereby validating the E-HIPA problem formulation. To cope with the second challenge, the proposed E-HIPA includes an adaptive orthogonal matching pursuit (AOMP) algorithm to adapt to the unknown number of targets. We show that AOMP can recover the location vector correctly with high probability.

Note that locating intensive multiple targets distorting the same link remains a challenging problem [13]. E-HIPA also presumes that any two targets are located sparsely, similar to existing DFL approaches [8], [11], [17]. This assumption is easy to satisfy in practice, since the sensing range of a link is limited, i.e., the effective nonzero RSS changes distorted by a target are limited to a finite region, please refer to Section 3.2 for details.

5. We divide the monitoring area into N grids and utilize these grids to represent the locations of K targets, as illustrated in Fig. 1d, where $N = 30$ is much larger than $K = 2$. Thus, the location vector Θ is a 2-sparse signal over the monitoring area that is divided into 30 grids.

2 Related Work

Early DFL work rely on camera [19] or infrared analysis [20]. Typically, they utilise video or thermo-image to detect and localize target(s). However, those approaches either largely depend on daylight or do not penetrate smoke. Recently, some RF-based DFL systems, such as WiTrack2.0 [7], and Tadar [12], have been proposed. They do not require floodlights to work at night, and can localize people in a smoke-filled building, or from the exterior of a building. However, these systems all demand dedicated hardware, such as USRP software defined radios with specialized signals (i.e., frequency modulated carrier wave) [7] or special RFID reader with a large number of tag arrays [12], which limits their application in some scenarios. This study utilises RSS for DFL, since the RSS readings are readily available in existing commercial off-the-shelf transceivers which are cheaper.

The concept of the RSS-based DFL was developed in the seminal work by Youssef et al. [13], who explicated the RSS changes to localize the target(s) and the modeled DFL problem as a fingerprint matching (location matched with the RSS changes) problem. RASS [11] is one of the most widely used fingerprinting based approaches, since it has sparse triangular deployment which can be scaled easily and is cost effective. However, RASS fails in multi-target DFL even when targets located sparsely in the same triangle, since RASS combines distortions from all the targets to locate a single "equivalent" target and treats multiple targets as a single target [11]. SCPL [21] is another popular fingerprinting based method. Compared with RASS, SCPL utilises the temporal transitions in human trajectories to improve the localization accuracy. RTI-based approaches [8], [17] localize the multiple targets by imaging the RSS attenuations across all the links and achieve an improved localization accuracy even if the targets remain stationary. However, the improvement of RTI-based approach comes at the expense of increased transmission volume and high energy consumption, since RTI deploys many transceivers and requires pair-wise transmissions.

Although some CS-based DFL methods have been proposed [22], [23]. However, these proposals have fundamental limitations that render them impractical. Specifically, none of these methods reduce the energy consumption, since they are based on the RTI's framework, which requires lots of transceivers to communicate with each other. Additionally, to estimate the location vector of multiple targets, these past CS-based DFL proposals either assume the availability of the number of targets (i.e., the sparsity level) with the orthogonal matching pursuit (OMP) algorithm [24] and etc, or they suffer from high computational complexity with the sparsity adaptive matching pursuit (SAMP) algorithm [25] which estimates the sparsity level (i.e., the target number) by many repeated iterations. However, the number of targets (or sparsity level) is not available in the localization problem, and the high computational complexity of SAMP makes these CS-based DFL proposals cannot scale when the size of monitoring area or the number of targets increased.

Given the limitations of previous work, this paper presents E-HIPA, a new CS-based DFL to localize sparse multiple targets accurately with only a small number of measurements (or transceivers). Unlike past CS-based DFL proposals, E-HIPA first re-examines the minimum number of measurements (or transceivers) required for multi-target DFL (by leveraging the CS theory). Thus, E-HIPA can reduce the number of transceivers deployed in a monitoring area, which results in an energy-efficiency. Secondly, we design an adaptive orthogonal matching pursuit (AOMP) algorithm for E-HIPA's Framework, by which E-HIPA is capable of recovering the precise location vector with high probability, even for a more practical scenario with unknown target number. Another important feature of E-HIPA is that AOMP can fast estimate the location vector of multiple targets. Since compared with SAMP, AOMP has a lower computational complexity which is more efficient for solving the localization problem.

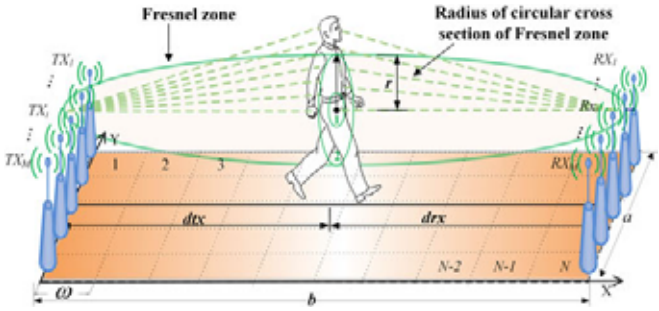

Fig. 2. A deployment view.

3 The Design of E-HIPA

The design of E-HIPA for localizing multiple targets based on the CS theory is not trivial with two primary challenges. The first is how to establish a sensing matrix which satisfies the RIP, so that we can formulate the DFL problem as a standard framework of the CS-based sparse recovery problem. The second is the design of a recovery algorithm which can adapt to an unknown number of targets, so that the formulated CS-based DFL problem is solvable in practical applications.

3.1 System Model and E-HIPA Problem Formulation Based on Compressive Sensing

When the radio signals propagate in the monitoring area, the targets within the area diffract, scatter, absorb or reflect some of the transmitted signal. Due to the unique propagation properties of electromagnetic waves, the distorted RSS measurements vary when the target is at different locations. Thus, one can utilize these distorted RSS measurements to localize the target(s) without requiring devices attached on target(s) [8], [11], [13], [26], [27].

Considering K targets randomly located in a monitoring area of size $a \times b$, and the area is divided equally into N grids with the side length ω. We divide $2M$ transceivers into a transmitter (TX) set $\{TX_1, \ldots, TX_i, \ldots, TX_M\}$ and a receiver (RX) set $\{RX_1, \ldots, RX_i, \ldots, RX_M\}$, which are then deployed on both sides of the monitoring, respectively. Each node is placed at the midpoint of a grid side, as illustrated in Fig. 2. Note that TX_i and RX_i construct a link, TX_1 and RX_M construct a link, and TX_M and RX_1 construct a link. Then, the total number of measurement links is $M + 2$. For simplicity, the number of links is approximated to M in the following problem formulation. Compared with the deployment for RTI, the deployed transceivers and links in this study are greatly reduced, as illustrated in Fig. 1c and 1d.

Here, we shall give a high level view about the RSS changes distorted by a target. Based on the wireless communications principles [28], the RSS measurement R_{ij} (in dB) of the link i ($1 \leq i \leq M$), given a single target locates at the grid j ($1 \leq j \leq N$), is described as

$$R_{ij} = P_i - L_i - D_{ij} - Q_i, \tag{1}$$

where P_i is the transmission power of the link i, L_i is the radio propagation fading of the link i, due to the path loss and the antenna patterns, D_{ij} is the diffraction fading of the link i, due to a target located at the grid j (the grid j is within the Fresnel zone[6] of link i) that blocks the propagation path of the link i (e.g., the target in Fig. 2), which can decrease the received power, and Q_i represents other fading losses such as the multi-path effect and etc.

In this study, we use the distorted RSS change measurement to quantify the interference distorted by the target. R_{ij} and F_i denote the RSS measurements of the link i when a target is located at the grid j and is located outside the monitoring area (i.e., when the link i is not distorted), respectively. In a dynamic environment, on average P_i, L_i and Q_i will not change [29], and thus we can obtain the distorted RSS change measurement of the link i due to a target located at the grid j by

$$\Delta R_{ij} = R_{ij} - F_i = -D_{ij}. \tag{2}$$

As the monitoring area has been divided into N grids, the locations of the K targets are denoted by the vector

$$\boldsymbol{\Theta} = [\theta_1, \theta_2, \ldots, \theta_j, \ldots \theta_N]^T, \tag{3}$$

where $\theta_j \in \{0, 1\}$. If there is one target at the grid j, $\theta_j = 1$, otherwise, $\theta_j = 0$. Thus, the number of targets is $K = \sum_{j=1}^{N} \theta_j$. $\boldsymbol{\Theta}$ has a K-sparse nature in the spatial domain, usually the number of targets K is smaller than the number of grids N, i.e., $K < N$. For example, a $10\ \mathrm{m} \times 10\ \mathrm{m}$ room can be divided into $N = 400$ grids when $\omega = 0.5\ \mathrm{m}$, while the number of people K in this room will be smaller than 400 in most cases. Thus, only a small number of K elements of $\boldsymbol{\Theta}$ are nonzero, i.e., $\boldsymbol{\Theta}$ has a K-sparse nature.

Since $\boldsymbol{\Theta}$ is K-sparse, taking advantage of CS in sparse recovery, rather than measuring the N-dimensional K-sparse signal $\boldsymbol{\Theta}$ directly, RSS change measurements $Y_{M\times 1}$ in a low M-dimensional space[7] are conducted to recover the $\boldsymbol{\Theta}$ accurately. It implies that, on one hand we can reduce the energy consumption by deploying a few transceivers in the monitoring area, on the other hand we can achieve high-precision property by applying the CS theory to recover $\boldsymbol{\Theta}$ accurately with a small number of measurements (or transceivers). In a word, by reducing the number of transceivers and applying the CS theory, we can achieve both the energy-efficiency and high-precision properties. According to CS, we formulate the DFL problem as

$$Y_{M\times 1} = \mathrm{A}_{M\times N} \cdot \boldsymbol{\Theta}_{N\times 1} + n, \tag{4}$$

where $Y_{M\times 1} = [y_1, \ldots, y_i, \ldots, y_M]^T \in \mathbb{R}^M$, y_i is the RSS change value measured by link i in the localization phase, $\mathrm{A} \in \mathbb{R}^{M\times N}$ is the sensing matrix established in the pre-deployment phase, under which the measured RSS change vector $Y_{M\times 1}$ has the sparse location vector $\boldsymbol{\Theta}$, and $n \in \mathbb{R}^M$ is the measurement noise.

As we mentioned previously, one of the primary challenges in designing E-HIPA is to establish a sensing matrix which satisfies the RIP, so that we can formulate the DFL problem as a standard framework of the CS-based sparse recovery problem. We design such a sensing matrix in the pre-deployment phase. Here, let one target moves around the monitoring area, and then all the M links measure the RSS change value distorted by the target, or the fingerprints, for each of the N grids. In aggregate, the $M \times N$ fingerprints, which made by the N grids on the RSS change value measured by M links, make up the sensing matrix $\mathrm{A}_{M\times N}$. $\mathrm{A}_{M\times N}$ is defined as

$$\mathrm{A}_{M\times N} = \begin{bmatrix} \Delta R_{11} & \Delta R_{12} & \cdots & \Delta R_{1N} \\ \Delta R_{21} & \Delta R_{22} & \cdots & \vdots \\ \vdots & \vdots & \Delta R_{ij} & \vdots \\ \Delta R_{M1} & \cdots & \cdots & \Delta R_{MN} \end{bmatrix}, \tag{5}$$

where ΔR_{ij}, which is described in (2), is the RSS change measurement distorted by a target located at the grid j and measured by the link i.

The reasons that we choose the sensing matrix A in the form of (5) are as follows. First, based on (4), the measurement y_i is the sum of the inner product of the vector $\boldsymbol{\Theta}$ and the vector $\langle \mathrm{A}' \rangle_i$ (ith row of A). Note that, y_i also recodes the measurement when a target is located at an unknown location in the localization phase, and different unknown locations (or $\boldsymbol{\Theta}$) should be reflected by different measurements (or y_i). Thus, the ith row of A should involve all the prior knowledge (measured by the link i) when a target moves to different locations. Second, we can prove that the designed sensing matrix A obeys the RIP, as shown in Section 4.1. In summary, the sensing matrix A should be established according to the rule defined by (5).

Discussion: E-HIPA is built on the deployment setup of Fig. 2, where the monitoring area is a regular rectangle region and all the transceivers are deployed within a single-hop communication range. For an irregular monitoring area or a large monitoring area (which cannot be covered by a single-hop communication range), E-HIPA works as follows. Firstly, E-HIPA divides the irregular area or the large area into small rectangular subareas. For the boundaries of the irregular area, E-HIPA uses additional small rectangular subareas to cover them. Then, E-HIPA estimates the target locations simultaneously in each subarea.

3.2 Feasibility for Localizing Multiple Targets with the CS Theory

Here, we validate the feasibility of using the linear superposition in CS, i.e., $Y = \mathrm{A} \cdot \boldsymbol{\Theta}$, for locating multiple targets that are located sparsely.

Fig. 3 shows the results of a simple experiment when two targets (i.e., two people with height of about 1.8 m) are located in a 6 m $\times$ 6 m area. Based on the deployment setup

6. A Fresnel zone is one of a number of concentric ellipsoids, as shown in Fig. 2, which determines the volumes of the diffraction fading.

7. Each of the M links, as illustrated in Fig. 2, will provide one measurement in the localization phase. It is easy to get that $M < N$, based on the localization scene we described in Fig. 2.

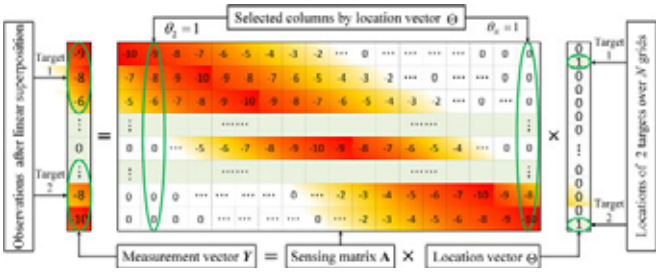

Fig. 3. The linear superposition behind the CS theory for multi-target DFL.

introduced in Section 3.1, We divided the area into $N = 144$ grids with ω=0.5 m. For simplicity, we let the two people stand at the second and last grid, respectively. If the localization vector Θ is estimated correctly, i.e., $\theta_2 = 1$, $\theta_N = 1$ and $\theta_j = 0$ ($j \neq 2$, $j \neq N$). Then, the second and last columns of sensing matrix A would be selected and linearly weighted by the location vector Θ.

In this study, we find that the sensing range of a link is limited, i.e., the effective nonzero RSS changes distorted by a target are limited to a finite region. Fig. 4 shows the distorted RSS values (*Z*-axis) when a target (a person with height of about 1.8 m) is located at different grids (*X*-axis and *Y*-axis) in the 6 m $\times$ 6 m monitoring area. Those RSS values are acquired from the link which crosses the center of the monitoring area. As we can see that (i) the distorted RSS values change dramatically when the target is located in the line-of-sight (LOS) between the two transceivers (along the *X*-axis direction); (ii) the distorted RSS changes are negligible when the target is located at the locations more than 0.75 m away from LOS between the two transceivers. The reason is that, according to the diffraction theory [28], the distorted RSS changes (i.e., the diffraction fadings) are large when target locates at the LOS path and blocks the first Fresnel zone[8]; while, the RSS changes are negligible when target far away from the transceivers and keeps the first Fresnel zones clear. It implies that most elements of A approximate to zero.[9]

Due to the spatial location difference of each link, the distributions of nonzero and zero RSS changes in each row of A are different, as shown in Fig. 3. For example, the first row of A, i.e., $\langle \mathrm{A} \rangle_1$, corresponding to the RSS changes measured by the $(i = 1)$th link which covers the grids with small index based on the deployment shown in Fig. 2. Thus, the left and right elements of $\langle \mathrm{A} \rangle_i$ are non-zeros and zeros, respectively, as shown in Fig. 3. It implies that the present of target 2 will not distort the linear superposition results of target 1, since the impact of target 2, i.e., $\theta_N = 1$ will be linearly weighted by the zeros of $\langle \mathrm{A} \rangle_1$. Due to the sparse spatial locations of

8. According to the diffraction theory [28], the radius of the circular cross section of Fresnel zone is given by $r = \sqrt{\xi \lambda d_{tx} d_{rx}/(d_{tx} + d_{rx})}$, where λ represents the wavelength, d_{tx} and d_{rx} are the distance from the target to TX and RX, respectively, as shown in Fig. 2, and ξ is the number of Fresnel zone. The maximum diameter of the first, second and third Fresnel zone (There is a maximum diameter (or radius) of Fresnel zone when $d_{tx} = d_{rx}$) in this experimental setup are 0.87 m (with ξ=1), 1.23 m (with ξ=2) and 1.5 m (with ξ=3), respectively. While, the effective RSS changes shown in Fig. 4 are limited to a narrow region with wide of about 1.5 m, which includes the area of first, second and third Fresnel zone. In summary, the effective RSS changes are limited to a finite region.

9. For a clear vision in Fig. 3, we set the elements, i.e., the RSS change values, of sensing matrix A as zero when its value is less than 1 dBm.

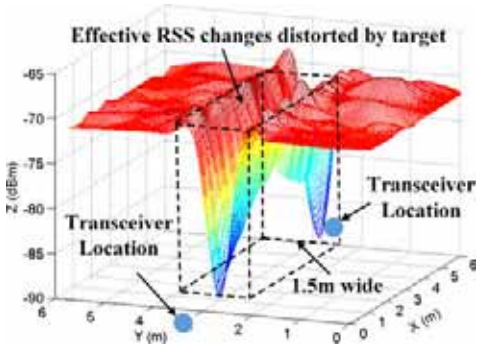

Fig. 4. RSS changes caused by target.

the two targets, the results of the linear superposition, i.e., the operation $\mathrm{A} \cdot \Theta$, are naturally divided into two parts. Intuitionally, the two partial results should equal/approximate to the measured RSS changes which are distorted by target 1 and target 2, respectively. Thus, the results of $\mathrm{A} \cdot \Theta$ equal/approximate to the measurement Y.

In summary, it is feasible to apply CS for localizing multiple targets that are located sparsely. However, locating multiple targets who distort the same link is a great challenge since the RSS changes distorted by multiple targets are non-linear superposition and it is still an open problem [28]. Thus, following most of the current DFL approaches [6], [8], [11], [27], E-HIPA will consider multiple targets as one target when they distort a same link. Note that, the assumption, i.e., we presume any two targets are located sparsely, is easy to satisfy, since the sensing range of a link is limited, i.e., the effective nonzero RSS changes distorted by a target are limited to a finite region.

3.3 E-HIPA Problem Solution by AOMP

To recover the location vector Θ from Y based on (4), we introduce the AOMP algorithm with low computational complexity which is capable of estimating Θ accurately without prior information of the number of targets K.

AOMP can estimate the sparsity level, i.e., the number of targets K, by using the Theorem 1 introduced later. As a consequence, AOMP can adapt to the target number to recover the location vector Θ accurately. In addition, inspired by the OMP algorithm which provides a low complexity by fast iteration, the recovery progress of AOMP is designed based on the basis of a modified OMP algorithm. Thus, AOMP also has a low computational complexity.

In the rest of this section, we first introduce Theorem 1 and then describe the detailed design of AOMP.

Definition 1. *Let $\Gamma = \{j : \theta_j \neq 0\}$ be the support of Θ. The actual number of nonzero components of Θ is $K = |\Gamma|$. Then K is referred to as the* actual sparsity level.

Definition 2. *Let $\Omega = \mathrm{A}^T Y$, and $\hat{\Gamma}$ be the support of the front $\hat{K}$ $(1 \leq \hat{K} \leq N)$ maximal values of Ω. The estimated number of nonzero components of Θ is $\hat{K} = |\hat{\Gamma}|$. Then $\hat{K}$ is referred to as the* estimated sparsity level.

Theorem 1. *Suppose that the sensing matrix* A *obeys the RIP with (K, δ), if $\hat{K} \geq K$, then we have*

$$||(\langle \mathrm{A} \rangle_j \mathbf{P}_{\hat{\Gamma}})^T Y||_{\ell_2} \geq \frac{1 - \delta}{\sqrt{1 + \delta}} ||Y||_{\ell_2}, \tag{6}$$

where, $\mathbf{P}_{\hat{\Gamma}}$ is the projection operator onto the orthogonal complement of the span of $\{\langle \mathrm{A} \rangle_j, j \in \hat{\Gamma}\}$, and δ is the constant in (13).

Proof. Suppose $K \leq \hat{K}$, then $\Gamma \subseteq \hat{\Gamma}$, thus we have

$$|(\langle \mathrm{A} \rangle_j \mathbf{P}_{\Gamma})^T Y||_{\ell_2} \leq ||(\langle \mathrm{A} \rangle_j \mathbf{P}_{\hat{\Gamma}})^T Y||_{\ell_2}. \tag{7}$$

Based on RIP, the singular value of $(\langle \mathrm{A} \rangle_j \mathbf{P}_{\Gamma})^T$ is between $\sqrt{1-\delta}$ and $\sqrt{1+\delta}$. Let $\lambda[(\langle \mathrm{A} \rangle_j \mathbf{P}_{\Gamma})^T (\langle \mathrm{A} \rangle_j \mathbf{P}_{\Gamma})]$ be the eigenvalues, then

$$1 - \delta \leq \lambda[(\langle \mathrm{A} \rangle_j \mathbf{P}_{\Gamma})^T (\langle \mathrm{A} \rangle_j \mathbf{P}_{\Gamma})] \leq 1 + \delta. \tag{8}$$

Thus, we have

$$\begin{aligned} \left\| (\langle \mathrm{A} \rangle_j \mathbf{P}_{\Gamma})^T Y \right\|_{\ell_2} &= \left\| (\langle \mathrm{A} \rangle_j \mathbf{P}_{\Gamma})^T (\langle \mathrm{A} \rangle_j \mathbf{P}_{\Gamma}) \Theta \right\|_{\ell_2} \\ &\geq (1-\delta) \|\Theta\|_{\ell_2}. \end{aligned} \tag{9}$$

Based on (13), it is easy to derive the following,

$$\|\Theta\|_{\ell_2} \geq \frac{\|\mathrm{A}\Theta\|_{\ell_2}}{\sqrt{1+\delta}} = \frac{\|Y\|_{\ell_2}}{\sqrt{1+\delta}}. \tag{10}$$

Hence, using (7), (9) and (10), we obtain

$$||(\langle \mathrm{A} \rangle_j \mathbf{P}_{\hat{\Gamma}})^T Y||_{\ell_2} \geq \frac{1-\delta}{\sqrt{1+\delta}} ||Y||_{\ell_2}. \tag{11}$$

□

Theorem 1 implies that if inequality (6) is satisfied with a given (or estimated) sparsity level $\hat{K}$, then $\hat{K}$ must be greater than or equal to the actual sparsity level K. Thus, Theorem 1 is a tool to estimate the sparsity level accurately.

Next, we introduce the AOMP algorithm, which is a two-stage algorithm. In the first stage, we estimate the sparsity level $\hat{K}$ by using Theorem 1, as shown in Lines 1-11 of Algorithm 1. To do so, we start with $\hat{K} = 1$, and increase $\hat{K}$ step by step (obviously, the updated $\hat{K}$ is closer to the actual sparsity level) until inequality (6) is satisfied. Then we can get the value of the estimated sparsity level $\hat{K}$. In the second stage, the estimated sparsity level $\hat{K}$ together with the measurement Y and the sensing matrix A are regarded as the input of a modified OMP algorithm, as shown in Line 12-21 of Algorithm 1. In simpler terms, we initially set all the elements of the estimated location vector $\hat{\Theta}$ as zero. Then, we find the index j of $\langle \mathrm{A} \rangle_j$ and the value of $\hat{\theta}_j$, which can minimize the correlation $\rho(j)$ at each iteration, as shown in Line 15 of Algorithm 1. Finally, all the elements of $\hat{\Theta}$ can be determined after N iterations.

Here, we discuss the computational complexity of AOMP. The running time of the AOMP algorithm is dominated by the loop related to j (Lines 14-20) whose complexity is $O(KMN)$. The estimation of sparsity level (Lines 1-11) leverages the binary search method, introducing a complexity of $O(\log(2N))$ [31]. Overall, the total complexity of the AOMP algorithm is $O(KMN + \log(2N))$. Compared with the SAMP algorithm [25], which can also recover a signal without requiring the sparsity level K, AOMP has a lower complexity. The complexities of the SAMP[10] in the worst and best cases are $O(MN^3)$ and $O(K^2MN)$, respectively. Thus, AOMP is more efficient than SAMP in recovering Θ because AOMP has a lower complexity.

Algorithm 1. Adaptive Orthogonal Matching Pursuit.

Input: The M dimensional measurement vector Y; The $M \times N$ dimensional sensing matrix A; The threshold level μ.
Output: The N dimensional reconstructed vector $\hat{\Theta}$.

1: $low = 1$, $high = N$, $\Omega = \mathrm{A}^T Y$;
2: **while** $low < high$ **do**
3: $\hat{K} = (low + high)/2$;
4: $\hat{\Gamma}$= {The index of the front $\hat{K}$ $(1 \leq \hat{K} \leq N)$ maximal values of $|\Omega|$};
5: **if** $||\langle \mathrm{A} \rangle_j \mathbf{P}_{\hat{\Gamma}} Y||_{\ell_2} < \frac{1-\delta}{\sqrt{1+\delta}} ||Y||_{\ell_2}$ **then**
6: $low = \hat{K} + 1$;
7: **else**
8: $high = \hat{K} - 1$;
9: **end if**
10: **end while**
11: $\hat{K} = high$;
12: $Res = Y$;
13: $\hat{\theta}_j = 0, \ \forall j \in \{1, 2, \ldots, N\}$;
14: **for** $j = 1$ to N **do**
15: $(j, \hat{\theta}_j) \leftarrow \underset{j \in \hat{\Gamma}, \hat{\theta}_j \in \{0,1\}}{\arg\min} \{\rho(j)\}$,
where $\rho(j) = \frac{||Res - (\langle \mathrm{A} \rangle_j \mathbf{P}_{\Gamma})^T Y'||_{\ell_2}^2}{||\mathbf{P}_{\Gamma} Y'||_{\ell_2}^2}$,
and $Y' = (\langle \mathrm{A} \rangle_j \mathbf{P}_{\hat{\Gamma}})[0, \ldots, \hat{\theta}_j, \ldots, 0]$;
16: **if** $\rho(j) \leq \mu$ **then** % Based on [30], we set threshold as $\mu = 2(1+\varepsilon)\log(N-K)/M$, where ε is a constant that is not too close to one.
17: $\hat{\Gamma} = \hat{\Gamma} \backslash \{j\}$;
18: $Res = Res - Y'$;
19: **end if**
20: **end for**
21: return $\hat{\Theta}$;

4 Theoretical Analysis

In this section, we provide theoretical analyses of three key aspects of E-HIPA. First, we validate the proposed CS-based framework problem formulation, i.e., the designed sensing matrix obeys RIP. Then, we prove that AOMP can recover the location vector Θ correctly with high probability, i.e., we demonstrate that E-HIPA can localize all targets accurately. Last, we show how to select the grid side length ω to achieve a high localization accuracy.

4.1 The RIP Constraint on Sensing Matrix A

Lemma 1. *The elements ΔR_{ij} of a row vector of sensing matrix A, i.e., $\langle \mathrm{A}' \rangle_i = \langle \Delta R_{i1}, \Delta R_{i2}, \cdots \Delta R_{ij} \cdots \Delta R_{iN} \rangle$, follow the Gaussian distribution.*

10. The SAMP divides the recovery process into several stages, and increases the sparsity level at each stage until it meets the stopping criterion (such as, the energy of the residual being less than a certain threshold). To recover a signal accurately, a simple but tedious scheme is to divide the process into N stages. However, in this case (the worst case, i.e., $\hat{K} = N$), the complexity of SAMP is $O(MN^3)$. An alternative scheme is to divide the process into exactly K stages. In this case (the best case, i.e., $\hat{K} = K$), the complexity of SAMP is $O(K^2MN)$.

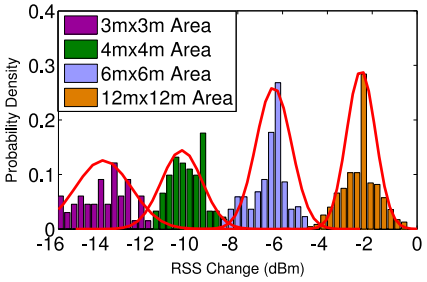

Fig. 5. Histogram plot of the RSS changes.

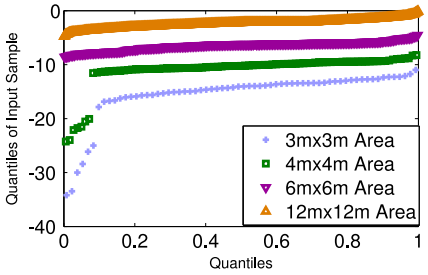

Fig. 6. Q-Q plot of the RSS changes.

Proof. This Gaussian distribution property is verified by checking the real-world experimental data. We conduct intensive experiments under different monitoring area sizes, i.e., 3 m × 3 m, 4 m × 4 m, 6 m × 6 m, and 12 m × 12 m. For a link of a particular area, we obtain the RSS changes when a target is located at different grids. Note that the RSS change values of each link comprise the rows of the sensing matrix. Fig. 5 shows that the RSS change measurements generally approximate the Gaussian distribution. However, the results from the histogram plot are a coarse-grained judgment, a more credible test is shown as follows.

The quantile-quantile (Q-Q) plot is one of the well known exploratory graphical method to check the Gaussian distributional assumption for a given data set. Fig. 6 shows the Q-Q plot of a row vector of sensing matrix A for different link lengths. As we can see that nearly all lines are close to a straight line, which indicates that the elements ΔR_{ij} $(1 \leqslant j \leqslant N)$ follow the Gaussian distribution. While, the validity of this determination may be influenced by personal views, since the Q-Q plot does not provide sufficient numerical criteria to make the determination.

The Jarque-Bera test is another commonly used method for testing whether a data set is drawn from the Gaussian distribution. The Jarque-Bera criterion is defined as

$$JB = n[S_k^2/6 + (K_u - 3)^2/24], \tag{12}$$

where, n is the size of the data set, S_k and K_u are the skewness and kurtosis,[11] respectively. For an ideal Gaussian distribution, JB follows the chi-square distribution with freedom of two degrees, i.e., $JB \sim \chi^2(2)$. For a given significance level, if the calculated JB is less than the critical value of $\chi^2(2)$, then the elements ΔR_{ij} of the vector $\langle \mathrm{A}' \rangle_i$ are accepted as following the Gaussian distribution, otherwise, they are rejected [32]. Fig. 7 shows that the calculated JB is less than the critical value of $\chi^2(2)$ when the significance level is greater than 0.05. In other words, the elements ΔR_{ij} of the vector $\langle \mathrm{A}' \rangle_i$ follow the Gaussian distribution with a significance level of at least 0.05. □

Theorem 2. *When the number of RSS change measurements (or links) $M = O(K\log(N/K))$, the probability for sensing matrix* A *(after normalization) to satisfy*

$$1 - \delta \leq \|A\Theta\|_{\ell_2}^2 / \|\Theta\|_{\ell_2}^2 \leq 1 + \delta, \tag{13}$$

for a K-sparse vector Θ tends to 1 (i.e., A *obeys RIP), where δ is a constant that is not too close to one.*

11. The definition of S and K are provided in work [32].

Proof. Consider a row vector of sensing matrix A:

$$\langle \mathrm{A}' \rangle_i = \eta \langle \Delta R_{i1}, \Delta R_{i2}, \cdots \Delta R_{ij} \cdots \Delta R_{iN} \rangle, \tag{14}$$

where ΔR_{ij} satisfies the Gaussian distribution with mean of u_0 and variance of δ_0, as proved in Lemma 1. Here, η is the normalization constant, which is expressed as

$$\eta = 1/(\sigma_0 \sqrt{M}). \tag{15}$$

Since all the K targets are randomly distributed in the area, the product of $\langle \mathrm{A}' \rangle_i$ and the K-sparse vector Θ, i.e., $\langle \mathrm{A}'\Theta \rangle_i$, follows the Gaussian distribution with the mean of u and the following variance

$$\sigma^2 = \eta^2 \cdot \sigma_0^2 \cdot \sum_{h=1}^{k} \theta_h^2, \tag{16}$$

where θ_h $(1 \leq h \leq K)$ is the hth nonzero element of Θ. As such, $\|\mathrm{A}\Theta\|_{\ell^2}^2$ satisfies χ^2-distribution (the degree of the freedom is M) with the mean of $M\sigma^2$ and the variance of $2M\sigma^4$. Since $M \gg 1$, $\|\mathrm{A}\Theta\|_{\ell^2}^2 / \|\Theta\|_{\ell^2}^2$ can be approximated by the Gaussian distribution with the following mean

$$M\sigma^2 \Big/ \sum_{h=1}^{K} \theta_h^2 = M \cdot \eta^2 \cdot \sigma_0^2 = 1, \tag{17}$$

and the variance of $2/M$. According to the Chernoff bound,

$$\Pr\left\{ \left| \|\mathrm{A}\Theta\|_{\ell^2}^2 / \|\Theta\|_{\ell^2}^2 - 1 \right| > \delta \right\} \leq 2\exp(-\delta^2 M/8). \tag{18}$$

Since the possible number of K-dimensional subspaces of A is $C_N^K \leq (eN/K)^K$, the probability that a K-sparse Θ which satisfies $|\|\mathrm{A}\Theta\|_{\ell^2}^2 / \|\Theta\|_{\ell^2}^2 - 1| > \delta$ is at most

$$\left(\frac{eN}{K}\right)^K \cdot 2\exp\left(-\frac{\delta^2 M}{8}\right) = 2\exp\left(-\frac{\delta^2 M}{8} + K\log\left(\frac{N}{K}\right) + 1\right). \tag{19}$$

Note that when $M = O(K\log(N/K))$, (19) tends to 0. Thus, the probability for (13) to be satisfied tends to 1. □

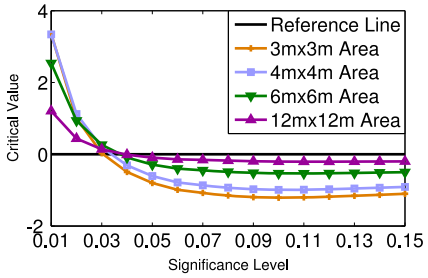

Fig. 7. Jarque-Bera test of the RSS changes.

Theorem 2 shows that the sensing matrix A designed in the form of (5) satisfies RIP, which is the basis to enable this CS-based framework problem formulation.

4.2 Accuracy Analysis of AOMP for Sparse Signal Recovery

Theorem 3. *When the number of links M satisfies $M = O(K\log(N/K))$ and the measurement noise n is power limited $E\|n\|^2 \leq 1$, AOMP can reconstruct Θ correctly with overwhelming probability for all large N.*

Proof. Let the correlation energy $\rho(j) = \|Res - (\langle A\rangle_j \mathbf{P}_\Gamma)^T Y'\|_{\ell_2}^2 / \|\mathbf{P}_\Gamma^T Y'\|_{\ell_2}^2$, where Res is the energy of the residual, and Y' is defined in Line 15-17 of Algorithm 1. Let us consider the following two probabilities, i.e., the *missed detection* probability $p_{MD} = \Pr(\min_{j\in\Gamma}\rho(j) \leq \mu)$, and the *false alarm* probability $p_{FA} = \Pr(\max_{j\notin\Gamma}\rho(j) \geq \mu)$. The p_{MD} corresponds to the event in which the maximum correlation energy $\rho(j)$ of the correct vectors $j \in \hat{\Gamma}$ falls below the threshold. The p_{FA} corresponds to the maximum energy on one of the "incorrect" indices $j \notin \hat{\Gamma}$ exceeding the threshold. Then, the probability of the reconstruction error p_{err} can be expressed as $p_{err} = p_{MD} + p_{FA}$.

When $\mu = (1+\delta)\log(N-K)/(M-K)$ (where δ is the constant in (13)) and the noise n is power limited $E\|n\|^2 \leq 1$ (where n is the noise in (4)), it has been proven by Fletcher et al. [33] that $\min_{j\in\Gamma}\rho(j)/\mu > 1$, i.e., $p_{MD} = 0$. Thus, it is easy to get that $p_{err} = p_{FA}$ in this case. According to the literature [33], when $j \notin \Gamma$, $\rho(j)$ follows a Beta $B(2, 2(M-1))$ distribution. When M is large, this beta distribution approximates Rayleigh distribution and the false alarm probability is given by $p_{FA} \approx \exp(-\mu M)$. Therefore, when $\mu = (1+\delta)\log(N-K)/(M-K)$ and $M = O(K\log(N/K))$, we obtain the following

$$p_{FA} \approx \exp\left(-\frac{(1+\delta)\log(N-K)}{cK\log(N/K)-K}\cdot cK\log(N/K)\right) < \exp(-(1+\delta)\log(N-K)). \quad (20)$$

Note that $p_{FA} = 0$ in this case. Thus, when $N \to \infty$, $p_{err} = p_{FA}$ tends to 0, i.e., Θ can be reconstructed correctly. □

Theorem 3 shows that E-HIPA can localize targets accurately when AOMP meets the condition for recovering the sparse vector Θ correctly.

4.3 Conditions of High Localization Accuracy

Theorem 4. *The sufficient condition to reconstruct the location vector Θ correctly, i.e., without reconstruction error, is that the grid side length ω satisfies the following*

$$\sqrt{ab/K}10^{-0.5\sqrt{a/(bK)}} < \omega < \sqrt{ab/K}, \quad (21)$$

where K is the number of targets, and $a \times b$ is the size of monitoring area.

Proof. According to the CS theory [18], the minimum samples required to recover the sparse location vector Θ exactly, i.e., without reconstruction error, is $O(K\log(N/K))$. Thus, we obtain the following

$$M > K\log(N/K). \quad (22)$$

According to Section 3.1, $M = a/\omega$, and $N = ab/\omega^2$. Thus, (22) can be rewritten as follows

$$a/\omega > K\log[ab/(\omega^2 K)]. \quad (23)$$

It is difficult to obtain the explicit and exact solutions of the above inequality, so we find out the approximate solutions of (23). Note that the number of targets K is usually smaller than the number of grids N, i.e., $K < N = ab/\omega^2$. Thus,

$$\omega < \sqrt{ab/K}. \quad (24)$$

It is easy to derive that $a/\omega > a/\sqrt{ab/K}$. Thus, if ω satisfies the following inequality

$$a/\sqrt{ab/K} > K\log[ab/(\omega^2 K)], \quad (25)$$

then ω must also satisfy (23). Taking (24) and (25) into account, we have

$$\sqrt{ab/K}10^{-0.5\sqrt{a/(bK)}} < \omega < \sqrt{ab/K}. \quad (26)$$

□

By Theorem 4, one can set a suitable side length ω to ensure that E-HIPA achieves high localization accuracy.

Fig. 8. The real world scene.

5 Performance Evaluation

5.1 Experimental Setup

We conduct extensive real-world experiments to validate the effectiveness of E-HIPA in a 6 m × 6 m monitoring area. We arrange eight people who act as the targets. Note that the number of test grids increases as the side length ω decreases. To enrich our experiments, we attempt to determine the minimum ω that satisfies (22), i.e., the lower bound of the exact solutions of Theorem 4. By our best efforts, we set ω=0.5 m, where $M = a/\omega = 12 > K\log[ab/(\omega^2 K)] \approx 10.04$. The transceivers used in our experiments are the MICAZ [34] nodes. Each TX node transmits one packet every 100 millisecond. We connect one node to a notebook via an MIB520 [34] to act as the sink, as shown in Fig. 8.

To localize the target(s), E-HIPA has two phases: establishing the sensing matrix in the pre-deployment phase and localizing the target(s) in the online phase. (i) *Establishing the sensing matrix:* Before the multiple targets enter the monitoring area, the link i $(1 \leq i \leq M)$ records RSS

TABLE 1
Default Values of Experimental Parameters

Parameters	Default Values
The number of targets K	8
The number of links M	12
The length of grid side ω	0.5 m
The length of link b	6 m
The size of monitoring area As	6 m $\times$6 m

measurements for 0.5 minutes, and the mean of those scans is denoted as F_i. Then we ask one person to go through all the N grids of the monitoring area. In the area, link i records RSS measurements for 0.5 minutes when a person is located at grid j, and the mean of those measurements is denoted as R_{ij}. Then, the sensing matrix A can be obtained by (2) and (5). (ii) *Localizing the target(s):* In the monitoring area, K people randomly stand at K different grids. Unlike most existing work [8], [11], [13], [26], [27] that assume the targets are located at the center of a grid, the targets in our experiment are randomly positioned within the grid which reflects a more realistic scenario. All the M links records RSS samples for 0.5 minutes. For the link i, we use the difference between the mean of the current measurements and the F_i as the i^{th} element of $Y_{M\times 1}$. Finally, at the notebook, we estimate the locations of the K people using the AOMP algorithm.

5.2 Comparison and Metric

Compared approaches. We implement three state-of-the-art methods for comparison, i.e., the RTI method [8], the SCPL method [21] and the RASS method [11]. Note that, (i) RTI estimates the location of a target with an image area rather than an exact grid, thus we consider the center grid of the imaged area as the exact location; (ii) we use a 2 order trajectory ring for SCPL as suggested in [21]; (iii) RASS fails to localize multiple targets even when targets located sparsely in the same area [11], thus we let the targets enter the area sequentially (with short time separation), and conduct localization for different targets as successive events in time. We also test the ability of AOMP in sparse recovery by comparing with two well-known CS recovery algorithms including OMP [24] and SAMP [25]. Note that OMP requires the availability of the sparsity level K, which is an unknown parameter in this study. Therefore, we tailor OMP by changing its exit condition from "iterating K times" to "iterating until the residual is smaller than a threshold ($< 10^{-3}$)".

Performance metric. The performance metric is the localization error, i.e., the distance between the true location and the estimated location. Let K be the actual number of targets with locations $(x_1, y_1), (x_2, y_2), \ldots, (x_K, y_K)$. Suppose that the corresponding estimated locations are (x'_1, y'_1), (x'_2, y'_2), $\ldots$, $(x'_{\hat{K}}, y'_{\hat{K}})$, where $\hat{K}$ is the estimated target number. Let $K_{\min} = \min\{K, \hat{K}\}$. To assign an estimated location to a target, we compute all pairs of the distance between (x_k, y_k) and (x'_k, y'_k), where $1 \leqslant k \leqslant K_{\min}$. We then sort these in a nondecreasing order and assign a target to the first unused estimated location. Then the localization error is expressed as

$$Error = \frac{\sum_{k=1}^{K_{\min}} \sqrt{(x_k - x'_k)^2 + (y_k - y'_k)^2}}{K_{\min}}. \quad (27)$$

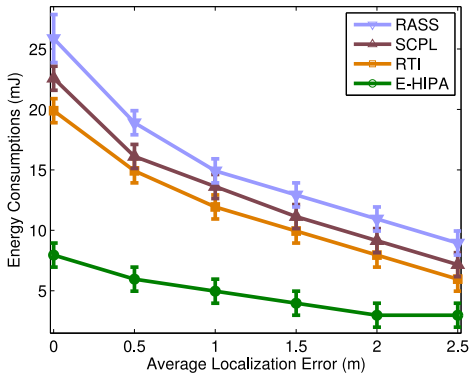

Fig. 9. Comparison of energy consumptions.

Also note that if E-HIPA regards multiple targets as one target, then we use the location of this equivalent one as the estimated locations for the multiple targets.

We evaluate performance by adjusting the following parameters: (i) K: the number of targets, (ii) M: the number of links, (iii) ω: the length of grid side, (iv) b: the length of link, (v) As: the size of monitoring area. Unless specifically mentioned, the default values are shown in Table 1. In the following figures, E-HIPA-OMP (or E-HIPA-SAMP) indicates the proposed CS-based framework problem formulation with OMP (or SAMP) as solution, since this CS-based framework problem formulation requires the CS recovery algorithm to estimate the target locations. Note that, E-HIPA includes AOMP, as we mentioned previously.

5.3 Comparison of Energy Consumption and Localization Accuracy

1) Comparison of energy consumption: First, we compare the energy consumption among E-HIPA, RTI, SCPL and RASS under a given localization accuracy. For each method, we increase the number of links until the localization accuracy reaches a given value, and then calculate the energy consumption. Based on the first order radio model [35], the energy consumption for each link is calculated as $E_{radio} = e_l B b^2 + 2BE_{elc}$, where B is the size of a packet in bits, b is the link length, e_l=100 pJ/(bit/m^2), and E_{elc}=50 nJ/bit. In our experiments, $B = 320$ bits, $b = 6$ m and each link repeatedly send and receive 30 packets in one localization phase. Thus, the energy consumption for a given method with M links is $M \times 0.99$ mJ. Fig. 9 shows the energy consumption for different average localization error values. To achieve a given accuracy, E-HIPA consumes the least energy, while RTI, SCPL and RASS consume more energy. For example, when the targets are localized accurately (i.e., when the localization error is 0), compared with RTI, SCPL and RASS, the proposed E-HIPA reduces the energy consumption by approximately $60\%(=\frac{20-8}{20}\times 100\%)$, $65\%(=\frac{23-8}{23}\times 100\%)$ and $69\%(=\frac{26-8}{26}\times 100\%)$, respectively. The reason is that E-HIPA employs CS to localize targets accurately with just a small number of measurements, while RTI, SCPL and RASS require more measurements for an accurate localization. Fig. 9 also shows that the energy consumption increased as the localization error decreased. The reason is that the number of links increases, the localization error decreases, as shown in Fig. 12 which will be discussed later.

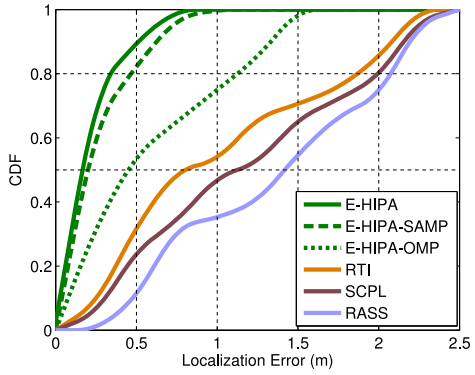

Fig. 10. Localization performance.

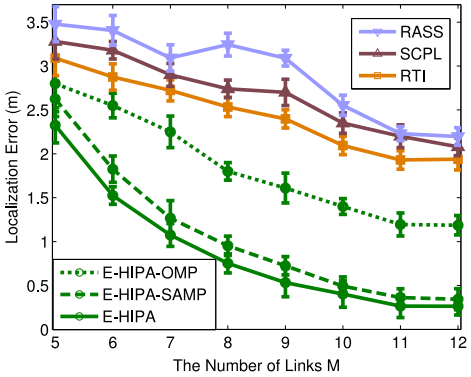

Fig. 12. Impact of link count.

2) Comparison of localization accuracy: Fig. 10 shows the cumulative distribution function (CDF) of the localization errors for E-HIPA, RTI, SCPL and RASS. E-HIPA performs the best with 50th and 80th percentile errors of 0.3 m and 0.4 m, respectively, while RTI, SCPL and RASS yield a large error with values of 1.7 m (80th percentile), 1.9 m (80th percentile) and 2.1 m (80th percentile), respectively. The reason why RTI does not perform as well is that (i) RTI requires a denser deployment to collect sufficient measurements to localize the targets accurately, and (ii) RTI estimates the location of a target with an area rather than an exact location [8]. The poor performance of RASS is primarily because RASS fails to localize multiple targets even when targets located sparsely in the same triangle. RASS combines all distortions from the K targets to locate a single "equivalent" target [11]. Since we let the targets enter the area sequentially, the localization errors would increase with the increased number of targets, as shown in Fig. 11. The performance of SCPL is similar to RASS since both of them are fingerprinting based approach. While, SCPL utilises the temporal transitions in target trajectories to improve the localization accuracy.

This experiment investigates how many targets can be localized accurately by E-HIPA. We increase the number of targets K from 2 to 16 with a step size 2, while other parameters use the default values. As we can see in Fig. 11, the maximum number of targets that can be localized accurately by E-HIPA depends on the number of links, i.e., under the restriction $M > K(\log(N/K))$. For example, when $K > 10$, the number of links required is $K(\log(N/K)) \approx 12.58$, which is greater than what we deployed in this scenario. For the similar reason in the previous paragraph, E-HIPA outperforms the RTI, SCPL and RASS methods.

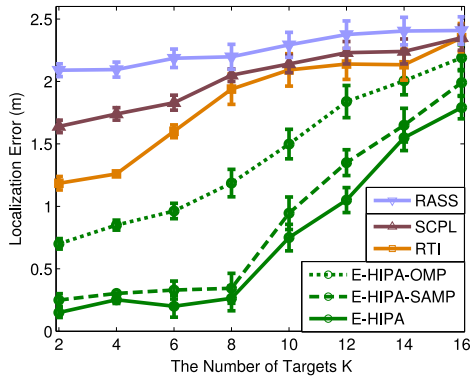

Fig. 11. Impact of target count.

Here, we evaluate the feasibility of sparser deployment. We decrease the number of links M from 12 to 5, by randomly removing the links deployed on two sides of the monitoring area, while other parameters use the default values. As shown in Fig. 12, compared with the default deployment scenario, the results indicate that E-HIPA supports sparser deployment with a particular number of targets, e.g., the localization error of E-HIPA still maintains a smaller value when $M = 11 < 12$, as it still satisfies $M = 11 > K(\log(N/K)) = 10.04$ according to the CS theory. The poor performance of RTI, SCPL and RASS is due to the same reason in the previous paragraph.

3) Comparison of sparse recovery capabilities: We now report our comparative study of AOMP vs. SAMP [25] and OMP [24]. We evaluate the performance of these three algorithms in solving the proposed CS-based framework problem formulation with different link counts and target counts. As can be seen in Fig. 12 and Fig. 11, AOMP (i.e., E-HIPA) is superior in terms of localization error compared with OMP (i.e., E-HIPA-OMP); while, compared with SAMP (i.e., E-HIPA-SAMP), the accuracy of AOMP is not improved significantly. The poor performance of OMP is due to that OMP requires the availability of the sparsity level K, which is unknown in this scene. Although OMP can iterate until the residual is minimum, it may still encounter an incorrect sparsity level K which can lead to a large localization error. SAMP can estimate the sparsity level adaptively during the iterating, thus, it can perform as well as AOMP. Figs. 12 and Fig. 11 also show that the localization errors of the three algorithms increased with the increased number of targets K or the decreased number of links M. The reason for this is that the proposed CS-based DFL framework with these recovery algorithms could not satisfy the CS theory, i.e., (22) could not be satisfied, when K increased or M decreased. Fig. 10 shows the CDF of the localization errors for AOMP, SAMP and OMP. Fig. 10 also illustrates that both AOMP and SAMP achieve high localization accuracy. However, AOMP suffers from high computational complexity. Fig. 13 shows the running time for AOMP, SAMP and OMP under different target counts. We test this using Matlab 7.0 on a laptop (2.0 GHz CPU and 2 GB memory). Compared with AOMP, the running time of SAMP and OMP increase significantly, since they require more iterations to recover the sparse signal. Taking into account

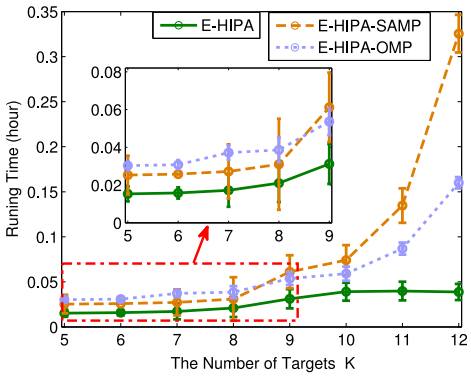

Fig. 13. Running time of recovery algorithm.

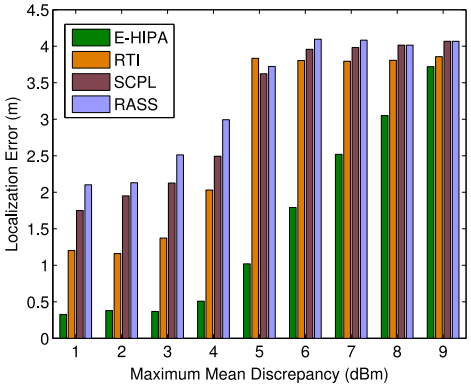

Fig. 14. Performance of new target.

the localization accuracy and the complexity, the AOMP algorithm demonstrates the best performance.

5.4 Robustness of E-HIPA

In this section, we evaluate the robustness of the E-HIPA method through the following two experiments.

This experiment investigates the robustness of E-HIPA when it localizes a new category of targets that are not used for modeling the sensing matrix. Usually, different categories or types of targets (such as tigers and monkeys) are always of disparate shapes, and hence yield a different RSS change measurements, even when they are located at the same location. To test robustness, we need to measure the difference of RSS change distributions across different target categories. For two given sets of RSS change measurements $\triangle R^1 = (r_i^1)$ and $\triangle R^2 = (r_i^2)$, where $r_i^1 \in \mathbb{R}^{n_1}$ and $r_i^2 \in \mathbb{R}^{n_2}$, this study uses the maximum mean discrepancy (MMD) [36], which can measure the distribution distance directly without density estimation, to quantify the difference in distributions. The distance is $dist(\Delta R^1, \Delta R^2) = ||\frac{1}{n_1}\sum_{i=1}^{n_1} r_i^1 - \frac{1}{n_2}\sum_{i=1}^{n_2} r_i^2||^2$, where $r_i^1 \in \Delta R^1$ and $r_i^2 \in \Delta R^2$.

A new target category means a new MMD across the existing target categories, thus, we only need to investigate how the differences of MMD among targets affect the localization performance. To mimic different MMDs among targets, we intend to add Gaussian noise with different means and variances to the RSS changes measurements $Y_{M\times 1}$ in (4). Fig. 14 shows the average localization errors for different MMD values. We observe that E-HIPA outperforms the other three schemes, no matter how much the MMD is increased. An interesting observation is that when the MMD is greater than 4 dBm, the localization error of E-HIPA increased linearly, while for the other two algorithms, the error remains nearly a constant large value. According to [37], if the measurement error or the noise is power-limited to ϵ, the reconstructed signal $\hat{\Theta}$ is guaranteed to be within $\delta\epsilon$ of the original signal Θ, i.e., $\|\hat{\Theta} - \Theta\|_{\ell_2} \leq \delta\epsilon$, where the constant δ depends only on the measurement parameters, not on the level of noise. MMD quantifies the bound of noise, therefore, the localization error of E-HIPA increases linearly as the MMD varies linearly.

All the experiments we conducted are with link length $b = 6$ m, i.e., the localization area is limited to 6 m $\times$ 6 m. To investigate the performance of E-HIPA under other link lengths and other area sizes, we conduct additional experiments (area size of 6 m $\times b$), with link length $b = 2$ m to $b = 16$ m with a step size 2 m. In each experiment, we use the same implementation and deployment settings described previously except for the link length. For a fair comparison, we normalize the localization error with the link length. Since these experiments require a significant amount of human efforts, we randomly test only 20 grids in each experiment due to time and resource constraints. Fig. 15 shows the average localization errors for eight link lengths. As can be seen, when the link length is less than 8 m, the errors of all the three methods are relatively stable and E-HIPA demonstrated the best performance. When the link length is greater than 10 m, large errors are observed for all methods for the following reasons. Fig. 16 (bottom) shows the standard deviation of RSS changes for different link lengths. We observe that the maximum standard deviation is less than 2 dBm, i.e., the noise is bounded under 2 dBm. Fig. 16 (top) shows the absolute RSS change measurement for different link lengths. As we can see that the absolute RSS change measurements distorted by the target decreased as the increase of link length. Due to the prorogation fading, the longer the link length is, the smaller the signal to noise ratio (SNR) is [28]. Thus, the small RSS changes will be absorbed by the noise when the link length is too long. For example in Fig. 16 (bottom), the absolute RSS change measurements are around 2 dBm when the link length is larger than 10m. The 2 dBm RSS changes would be mixed into the noise, thus these measurements cannot be used for localization. This experiment indicates that, for the given transmission power/transceivers, we should choose a suitable link length to guarantee the SNR for target localization.

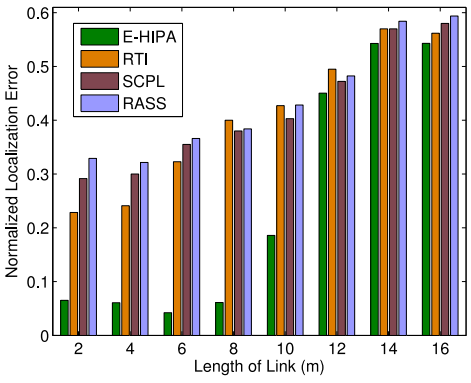

Fig. 15. Performance of other link lengths.

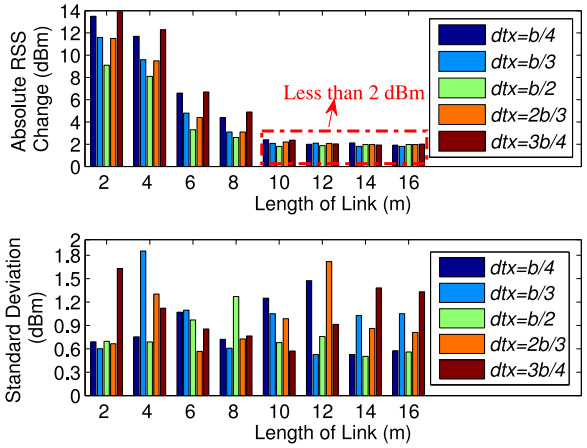

Fig. 16. Impact of link length on RSS changes.

5.5 Scalability of E-HIPA

To evaluate the scalability of E-HIPA, we increase the size of the localization area from 4 m $\times$ 4 m to 12 m $\times$ 12 m and the number of targets K from 5 to 30 with a sept of 5. As mentioned in Section 5.4, the link length is limited within 10 m when we using the MICAz nodes, which leads to a limited monitoring area. To deal with this problem, we use the approach discussed in the last paragraph of Section 3.1. For simplicity, we set the size of each subarea as 4 m $\times$ 4 m. Fig. 17 shows the average localization errors for different area sizes and target counts. It illustrates that the maximum area to which E-HIPA is applicable depends on the maximum number of targets. For example, when $K = 15$, the localization error increased drastically in the 4 m $\times$ 4 m area while the error remains small in the 8 m $\times$ 8 m area. The reason is that the maximum number of targets that can be localized precisely in each subarea is less than 10, since $Klog(N/K) \approx 8.1 > 8$ when $K = 10$, $N = (4/0.5)^2$. Therefore, the maximum number of targets can be localized precisely in 4 m $\times$ 4 m area and 8 m $\times$ 8 m area are 10 ($< K = 15$) and 20 ($> K = 15$), respectively.

These results indicate that the maximum area where E-HIPA is applicable depends on the maximum number of targets. Here, we analyse and discuss the scalability of E-HIPA. Based on the CS theory [18] and the experimental results shown in Fig. 11, there exists a maximum number K_{max} of targets that can be localized precisely in each subarea. Considering a large monitoring area which is divided into ξ subareas, thus the maximum number of targets (located randomly in the area) that can be localized precisely

Fig. 17. Scalability of E-HIPA.

TABLE 2
Experimental Parameters

	Subarea number (T)	Subarea size (A)	Subarea links number (M)	Subarea grids number (N)
Exp.1	1	12 m $\times$ 12 m	24	576
Exp.2	4	6 m $\times$ 6 m	12	144
Exp.3	9	4 m $\times$ 4 m	8	64
Exp.4	16	3 m $\times$ 3 m	6	36

is less than ξK_{max}. If the maximum number of targets in the monitoring area is less than ξK_{max}, E-HIPA can scale to any area size with high localization accuracy. Otherwise, the localization error has the following two characteristics: (i) if the area size is fixed, more targets lead to higher localization errors; and (ii) if the number of targets K is fixed, larger area sizes lead to lower localization errors, as illustrated in Fig. 17.

5.6 A Case Study

In this section, we illustrate an example of target localization using the generalized E-HIPA. In a 12 m $\times$ 12 m monitoring area, we conduct four experiments. For each experiment, we use T equal subareas to cover the monitoring area and deploy M links in each subarea. The grid side length $\omega = 0.5$ m. The experimental parameters are shown in Table 2.

Fig. 18 shows the localization results of the four experiments. Here, "Ture" indicates the true locations and "Exp. x" indicates the locations estimated in the xth experiment. The results of Exp. 3 and Exp. 4 illustrate that the generalized E-HIPA localize all the targtes accurately. While, the results of Exp. 1 and Exp. 2 demonstrate some large errors. The reason is that some of the links are distorted by more than one target in these two experiments. However, the distorted RSS of multiple targets are not linear additive [28], thus, E-HIPA cannot localize each of these targets accurately. For example, for the three collinear targets (the targets with coordinate of y = 6.25) in Exp. 1, E-HIPA consider them as one target and localize this "equivalent" target at (5.75, 6.25).

5.7 Tracking Targets by E-HIPA

The tracking scheme of E-HIPA is described as follows.

Firstly, we align the RSS change measurements of all the M links in accordance with the same time. For a set of RSS change time series measurements of each link, we then apply

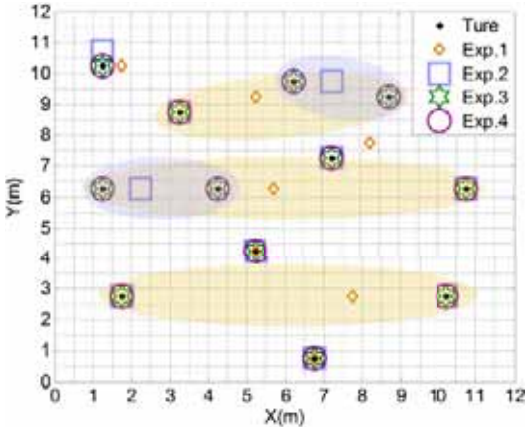

Fig. 18. Results of generalized E-HIPA.

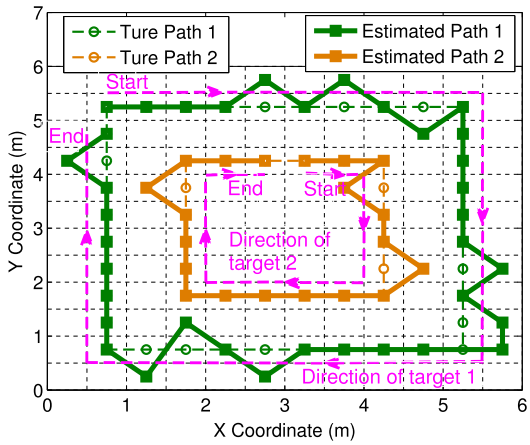

Fig. 19. Tracking results of two people.

a mean sliding window algorithm to filter noise. Let the measurements of link i over T moments be $\{y(i,1),\ldots, y(i,t),\ldots y(i,T)\}$. Then the output of the mean sliding window algorithm can be described as $\hat{y}(i,t)=\frac{1}{Q}\sum_{x=0}^{Q-1} y(i,t+x)$, where Q is the size of sliding window. Secondly, we run AOMP to estimate a set of location vectors $\{\Theta(t)\}$, $1\leq t\leq T$ with the corresponding pre-processed measurements $\{\hat{y}(i,t)\}$, $1\leq i\leq M$, $1\leq t\leq T$. Finally, we refine the estimated locations, since lots of the locations are repeated while a few of them are chaotic. To do so, we divide the set of location vectors $\{\Theta(t)\}$, $1\leq t\leq T$ into several blocks with the length of $|Q|$. In each block, we regard the highest frequency location as the final estimated location. At last, we arrange these final estimated locations in chronological order to get the trajectories of targets.

To evaluate the tracking performance of E-HIPA, we let two people with height of about 1.8 m move along different paths in the 6 m $\times$ 6 m monitoring area. The moving speed of the two people is about 0.5 m/s. We set Q as one second. Fig. 19 shows the estimated trajectories of the two people. As we can see that the tracking errors are under 1 m and most trajectories match the true paths well.

6 Conclusion and Future Work

This paper proposed E-HIPA, an energy-efficient framework for high-precision multi-target DFL. The goal of E-HIPA is to reduce energy consumption while providing precise localization of multiple targets without carried devices. We proved that the designed sensing matrix obeys RIP, which validates the CS-based framework problem formulation. To recover the location vector of targets under the restriction of unknown target number, E-HIPA includes a low computational AOMP algorithm to estimate the target locations accurately without prior information of the number of targets. Additionally, theoretical analyses were provided to validate the proposed problem formulation and solution. The experimental results illustrate the effectiveness and advantages of E-HIPA.

In the future work, we will try to relax the "located relatively sparsely" constraint for localizing multiple targets. The challenge lies in handling multiple targets who distort a same link. In this case, E-HIPA may regard them as one target due to the lack of effective analysis for single interference distorted by multiple targets. To the best of our knowledge, this problem is still an open issue [28]. One possibility is to assume that these entities will affect the area sequentially, and try to address them as successive events in time. This will require further research to determine how the environment is affected by the simultaneous and non-simultaneous changes due to multiple targets who are close to each other. We plan to develop probabilistic models to analyze such dynamic changes.

Acknowledgments

This work was supported in part by the National Key Technology R&D Program (2013BAK01B02), National Natural Science Foundation of China under Grants (61272461, 61572219, 61502192, 61572402, 61402372, 61373177), Natural Sciences and Engineering Research Council of Canada (NSERC), and Graduate Innovative Education Project of Northwest University YZZ14002. Xiaojiang Chen is the corresponding author.

References

[1] J. Wang and D. Katabi, "Rfid positioning that works with multipath and non-line of sight," in *Proc. ACM Sigcomm*, 2013, pp. 51–62.
[2] J. He, J. Chen, P. Cheng, and X. Cao, "Secure time synchronization in wirelesssensor networks: A maximumconsensus-based approach," *IEEE Trans. Parallel Distrib. Syst.*, vol. 25, no. 4, pp. 1055–1065, Apr. 2014.
[3] J. He, P. Cheng, L.-H. Shi, and J.-J. Chen, "Sats: Secure average-consensus-based time synchronization in wireless sensor networks," *IEEE Trans. Signal Process.*, vol. 61, no. 24, pp. 6387–6400, Dec. 2013.
[4] Y. Zhang, S. He, and J. Chen, "Data gathering optimization by dynamic sensing and routing in rechargeable sensor networks," *Proc. IEEE Sensor, Mesh Ad Hoc Commun. Netw.*, pp. 273–281, 2013.
[5] Y. Shu, G. S. Kang, T. He, and J. Chen, "Last-mile navigation using smartphones," in *Proc. ACM 21st Annu. Int. Conf. Mobile Comput. Netw.*, 2015, pp. 512–524.
[6] D. Zhang, K. Lu, R. Mao, Y. Feng, Y. Liu, Z. Ming, and L. Ni, "Fine-grained localization for multiple transceiver-free objects by using RF-based technologies," *IEEE Trans. Parallel Distrib. Syst.*, vol. 25, no. 6, pp. 1464–1475, Jun. 2014.
[7] F. Adib, Z. Kabelac, and D. Katabi, "Multi-person localization via RF body reflections," in *Proc. USENIX Conf. Netw. Syst. Design Implementation*, 2015, pp. 279–292.
[8] J. Wilson and N. Patwari, "See-through walls: Motion tracking using variance-based radio tomography networks," *IEEE Trans. Mobile Comput.*, vol. 10, no. 5, pp. 612–621, May 2011.
[9] C. Liu et al., "RSS distribution-based passive localization and its application in sensor networks," *IEEE Trans. Wireless Commun.*, vol. 15, no. 4, pp. 2883–2895, Apr. 2016.
[10] L. Chang, X. Chen, D. Fang, J. Wang, T. Xing, C. Liu, and Z. Tang, "Fale: Fine-grained device free localization that can adaptively work in different areas with little effort," *ACM Sigcomm Comput. Commun. Rev.*, vol. 45, no. 5, pp. 601–602, 2015.
[11] D. Zhang, Y. Liu, X. Guo, and L. M. Ni, "RASS: A real-time, accurate, and scalable system for tracking transceiver-free objects," *IEEE Trans. Parallel Distrib. Syst.*, vol. 24, no. 5, pp. 996–1008, May 2013.
[12] L. Yang, Q. Lin, X. Li, T. Liu, and Y. Liu, "See through walls with cots rfid system!" in *Proc. 21st Annu. Int. Conf. Mobile Comput. Netw.*, 2015, pp. 487–499.
[13] M. Youssef, M. Mah, and A. Agrawala, "Challenges: Device-free passive localization for wireless environments," in *Proc. Annu. Int. Conf. Mobile Comput. Netw.*, 2007, pp. 222–229.
[14] C. Li, C. Peng, S. Lu, and X. Wang, "Energy-based rate adaptation for 802.11 n," in *Proc. Annu. Int. Conf. Mobile Comput. Netw.*, 2012, pp. 341–352.
[15] X. Wang, S. Han, Y. Wu, and X. Wang, "Coverage and energy consumption control in mobile heterogeneous wireless sensor networks," *IEEE Trans. Autom. Cont.*, vol. 58, no. 4, pp. 975–988, Apr. 2013.
[16] J. Wilson and N. Patwari, "Radio tomographic imaging with wireless networks," *IEEE Trans. Mobile Comput.*, vol. 9, no. 5, pp. 621–632, May 2010.

[17] M. Bocca, O. K. Neal Patwari, and S. Venkatasubramanian, "Multiple target tracking with RF sensor networks," *IEEE Trans. Mobile Comput.*, vol. 13, no. 8, pp. 1787–1800, Aug. 2014.
[18] E. J. Candès and M. B. Wakin, "An introduction to compressive sampling," *IEEE Signal Process. Mag.*, vol. 25, no. 2, pp. 21–30, Mar. 2008.
[19] H. Ma, C. Zeng, and C. X. Ling, "A reliable people counting system via multiple cameras," *ACM Trans. Intell. Syst. Technol.*, vol. 3, no. 2, pp. 67–83, 2012.
[20] J. Kemper and D. Hauschildt, "Passive infrared localization with a probability hypothesis density filter, " in *Proc. Workshop Positioning Navig. Commun.*, 2010, pp. 68–76.
[21] C. Xu et al., "SCPL: Indoor device-free multi-subject counting and localization using radio signal strength," in *Proc. ACM/IEEE Int. Conf. Inform. Process. Sensor Netw.*, 2013, pp. 79–90.
[22] J. Wang, Q. Gao, X. Zhang, and H. Wang, "Device-free localisation with wireless networks based on compressive sensing," *IET Commun.*, vol. 6, no. 15, pp. 2395–2403, 2012.
[23] M. A. Kanso and M. G. Rabbat, "Compressed RF tomography for wireless sensor networks: Centralized and decentralized approaches," in *Proc. Distrib. Comput. Sensor Syst.*, 2009, pp. 173–186.
[24] D. L. Donoho, Y. Tsaig, I. Drori, and J.-L. Starck, "Sparse solution of underdetermined systems of linear equations by stagewise orthogonal matching pursuit," *IEEE Trans. Inf. Theory*, vol. 58, no. 2, pp. 1094–1121, Feb. 2012.
[25] T. T. Do, L. Gan, N. Nguyen, and T. D. Tran, "Sparsity adaptive matching pursuit algorithm for practical compressed sensing," in *Proc. Asilomar Conf. Signals, Syst. Comput.*, 2008, pp. 581–587.
[26] S. Sigg, M. Scholz, S. Shi, Y. Ji, and M. Beigl, "RF-sensing of activities from non-cooperative subjects in device-free recognition systems using ambient and local signals," *IEEE Trans. Mobile Comput.*, vol. 13, no. 4, pp. 907–920, Apr. 2014.
[27] M. Seifeldin, A. Saeed, A. Kosba, A. El-Keyi, and M. Youssef, "Nuzzer: A large-scale device-free passive localization system for wireless environments," *IEEE Trans. Mobile Comput.*, vol. 12, no. 7, pp. 1321–1334, Jul. 2013.
[28] A. F. Molisch, *Wireless Communications*. Hoboken, NJ, USA: Wiley, 2010, vol. 15.
[29] J. D. Jackson and L. Levitt, "Classical electrodynamics," *Amer. Inst. Phys.*, vol. 15, no. 11, pp. 62–62, 2009.
[30] A. K. Fletcher and S. Rangan, "Orthogonal matching pursuit from noisy measurements: A new analysis," in *Proc. Neural Inf. Process. Syst. Conf.*, 2009, pp. 1–9.
[31] R. D. Nowak, "The geometry of generalized binary search," *IEEE Trans. Inf. Theory*, vol. 57, no. 12, pp. 7893–7906, Dec. 2011.
[32] C. M. Jarque and A. K. Bera, "Efficient tests for normality, homoscedasticity and serial independence of regression residuals," *Elsevier Econ. Lett.*, vol. 6, no. 3, pp. 255–259, 1980.
[33] A. K. Fletcher and S. Rangan, "Orthogonal matching pursuit: A brownian motion analysis," *IEEE Trans. Signal Process.*, vol. 60, no. 3, pp. 1010–1021, 2012.
[34] T. Datasheet. (2012). "Crossbow Inc," [Online]. Available: http://www.xbow.com
[35] W. R. Heinzelman, A. Chandrakasan, and H. Balakrishnan, "Energy-efficient communication protocol for wireless microsensor networks," in *Proc. Int. Conf. Syst. Sci.*, 2000, pp. 10–20.
[36] M. Gangeh, A. Sadeghi-Naini, M. Diu, H. Tadayyon, M. Kamel, and G. Czarnota, "Categorizing extent of tumour cell death response to cancer therapy using quantitative ultrasound spectroscopy and maximum mean discrepancy," *IEEE Trans. Med. Imaging*, vol. 33, no. 6, pp. 1390–1400, Jun. 2014.
[37] E. J. Candes, J. K. Romberg, and T. Tao, "Stable signal recovery from incomplete and inaccurate measurements," *Commun. Pure Appl. Math.*, vol. 59, pp. 1207–1223, 2006.

Ju Wang received the BS degree in information engineering from Northwest University, Xi'an, China, in 2010, where he is currently working toward the PhD degree in the School of Information Science and Technology. His research interests include localization, Wi-Fi imaging, and signal processing.

Dingyi Fang received the BS and MS degrees in computer science from Northwest University, Xi'an, China, in 1983 and 1988, respectively. He received the PhD degree in computer application technology from Northwestern Polytechnical University of China, in 2001. He is currently a professor in the School of Information Science and Technology, Northwest University, Xi'an, China. His current research interests include mobile and distributed computing systems, network and information security, and wireless sensor networks.

Zhe Yang (S'09-M'13) received the BS degree in information engineering and the MS degree in control theory and engineering, both from Xi'an Jiaotong University, Xi'an, China, in 2005 and 2008, respectively. He received the PhD degree from the Department of Electrical and Computer Engineering, University of Victoria, British Columbia, Canada, in 2013. His research interests include cross-layer design, scheduling, and resources allocation for wireless networks. He is a member of the IEEE.

Hongbo Jiang received the BS and MS degrees from the Huazhong University of Science and Technology, China. He received the PhD degree from Case Western Reserve University in 2008. After that, he joined the faculty of Huazhong University of Science and Technology where he is now a full professor. His research concerns computer networking, especially algorithms and architectures for wireless networks and mobile computing. He is a senior member of the IEEE.

Xiaojiang Chen received the PhD degree in computer software and theory from Northwest University, Xi'an, China, in 2010. He is currently a professor in the School of Information Science and Technology, Northwest University. His current research interests include localization and performance issues in wireless ad hoc, mesh, and sensor networks and named data networks.

Tianzhang Xing received the BS degree in information engineering from Xidian University of Electronic Science and Technology, Xi'an, China, in 2004. He received the MS degree from Northwest University, Xi'an, China, in 2007. His research interests include signal processing, localization, and Internet of Things.

Lin Cai (S'00-M'06-SM'10) received the MASc and PhD degrees in electrical and computer engineering from the University of Waterloo, Waterloo, Canada, in 2002 and 2005, respectively. Since 2005, she has been with the Department of Electrical & Computer Engineering at the University of Victoria, and she is currently a professor. Her research interests span several areas in communications and networking, with a focus on network protocol and architecture design supporting emerging multimedia traffic over wireless, mobile, ad hoc, and sensor networks. She has received the NSERC Discovery Accelerator Supplement Grants in 2010 and in 2015, and the best paper awards of IEEE ICC 2008 and IEEE WCNC 2011. She has served as a TPC symposium co-chair for IEEE Globecom'10 and Globecom'13, and the associate editor for the *IEEE Transactions on Wireless Communications, IEEE Transactions on Vehicular Technology, EURASIP Journal on Wireless Communications and Networking, International Journal of Sensor Networks, and Journal of Communications and Networks (JCN).* She is a senior member of the IEEE.